Satellite Estimates of Mode-1 M_2 Internal Tides Using Nonrepeat Altimetry Missions

ZHONGXIANG ZHAO[a]

[a] *Applied Physics Laboratory, University of Washington, Seattle, Washington*

(Manuscript received 4 December 2021, in final form 28 July 2022)

ABSTRACT: Previous satellite estimates of internal tides are usually based on 25 years of sea surface height (SSH) data from 1993 to 2017 measured by exact-repeat (ER) altimetry missions. In this study, new satellite estimates of internal tides are based on 8 years of SSH data from 2011 to 2018 measured mainly by nonrepeat (NR) altimetry missions. The two datasets are labeled ER25yr and NR8yr, respectively. NR8yr has advantages over ER25yr in observing internal tides because of its shorter time coverage and denser ground tracks. Mode-1 M_2 internal tides are mapped from both datasets following the same procedure that consists of two rounds of plane wave analysis with a spatial bandpass filter in between. The denser ground tracks of NR8yr make it possible to examine the impact of window size in the first-round plane wave analysis. Internal tides mapped using six different windows ranging from 40 to 160 km have almost the same results on global average, but smaller windows can better resolve isolated generation sources. The impact of time coverage is studied by comparing NR8yr160km and ER25yr160km, which are mapped using 160-km windows in the first-round plane wave analysis. They are evaluated using independent satellite altimetry data in 2020. NR8yr160km has larger model variance and can cause larger variance reduction, suggesting that NR8yr160km is a better model than ER25yr160km. Their global energies are 43.6 and 33.6 PJ, respectively, with a difference of 10 PJ. Their energy difference is a function of location.

SIGNIFICANCE STATEMENT: Our understanding of internal tides is mainly limited by the scarcity of field measurements with sufficient spatiotemporal resolution. Satellite altimetry offers a unique technique for observing and predicting internal tides on a global scale. Previous satellite observations of internal tides are mainly based on 25 years of data from exact-repeat altimetry missions. This paper demonstrates that internal tides can be mapped using 8 years of data made by nonrepeat altimetry missions. The new dataset has shorter time coverage and denser ground tracks; therefore, one can examine the impact of window size and time coverage on mapping internal tides from satellite altimetry. A comparison of models mapped from the two datasets sheds new light on the spatiotemporal variability of internal tides.

KEYWORDS: Internal waves; Topographic effects; Sea level; Tides; Altimetry

1. Introduction

In the stratified ocean, the barotropic tidal current flowing over rough topographic features scatters a fraction of the tidal energy to baroclinic oscillations, which propagate away as internal tides (Wunsch 1975; Egbert and Ray 2000; Garrett and Kunze 2007; Arbic et al. 2018). Internal tides have numerous generation sites over seamounts, submarine ridges, and continental slopes in the global ocean. Internal tides propagate over hundreds to thousands of kilometers from their generation sites. Therefore, the internal tide signal at any given site in the ocean may contain multiple waves of different propagation directions (Zhao et al. 2019). In propagation, internal tides are modulated by seasonal stratification, large-scale ocean circulation, and mesoscale eddies (Ray and Zaron 2011; Zaron and Egbert 2014; Ponte and Klein 2015; Kelly et al. 2016; Dunphy et al. 2017; Zaron 2019b; Zhao 2021). Therefore, the global internal tide field is subject to significant spatial and temporal variations. Internal tides contribute about half of the energy required for mixing the ocean interior and maintaining ocean stratification. They play an important role in various ocean processes such as ocean acoustics, water mass formation, and tracer transport (Jayne and St. Laurent 2001; Cacchione et al. 2002; Rudnick et al. 2003; MacKinnon et al. 2017; Sasaki et al. 2018; Vic et al. 2019; Whalen et al. 2020). Long-range internal tides offer a promising tool for monitoring ocean changes (Zhao 2016). Thus, it is important to study their generation, propagation, and dissipation in the global ocean. Internal tides have been an active research topic in recent years (MacKinnon et al. 2017; Whalen et al. 2020). The knowledge of internal tides has been greatly improved, due to concerted theoretical, modeling, and observational efforts (Buijsman et al. 2020; de Lavergne et al. 2020; Kelly et al. 2021; Li and von Storch 2020; Löb et al. 2020; Olbers et al. 2020; Pollmann et al. 2019; Savage et al. 2020; Shakespeare 2020; Vic et al. 2021; Zhao 2021). Among them, satellite altimetry observes the global two-dimensional internal tide field from space, thanks to its near-global coverage (Dushaw 2015; Ray and Zaron 2016; Zhao et al. 2016; Zaron 2019a; Ubelmann et al. 2022).

Previous estimates of internal tides from satellite altimetry are usually based on about 25 years of SSH measurements made by exact-repeat altimetry missions since 1992 (Zhao 2019; Zaron 2019a; Ubelmann et al. 2022). The exact-repeat missions have sparse ground tracks and large intertrack spacing (section 2). For example, TOPEX/Poseidon has only

Supplemental information related to this paper is available at the Journals Online website: https://doi.org/10.1175/JPO-D-21-0287.s1.

Corresponding author: Zhongxiang Zhao, zzhao@apl.uw.edu

DOI: 10.1175/JPO-D-21-0287.1

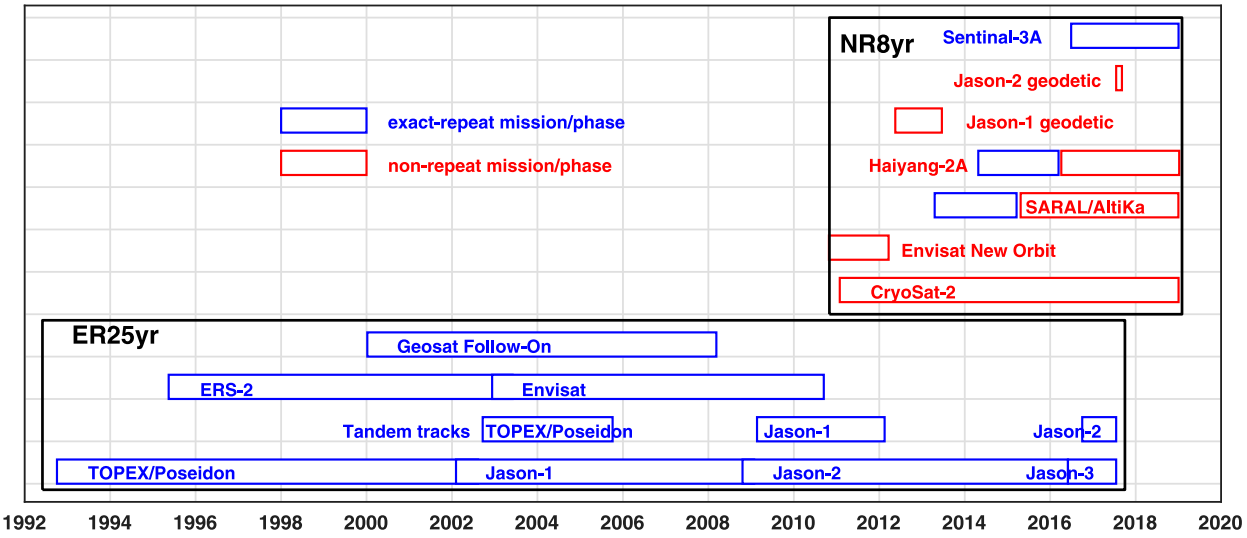

FIG. 1. The time coverage of satellite altimetry data used in this study. Exact-repeat (ER) and nonrepeat (NR) missions (phases) are in blue and red, respectively. The two datasets are labeled ER25yr and NR8yr, meaning that their time coverages are 25 and 8 years long, respectively.

254 ground tracks and its intertrack spacing is about 315 km at the equator, much larger than the typical 150-km wavelength of mode-1 M_2 internal tides. The merged dataset from seven exact-repeat missions has a total of 1998 ground tracks. Using the TOPEX/Poseidon data (254 ground tracks), Ray and Cartwright (2001) map mode-1 M_2 internal tides using 3° latitude × 4° longitude windows. Using the TOPEX/Poseidon data from both the original and interleaved phases (508 ground tracks), Zhao and Alford (2009) map mode-1 M_2 internal tides using 250-km windows. Using the seven-mission merged dataset (1998 ground tracks), Zhao et al. (2016) map M_2 internal tides in 160-km windows. In these studies, the M_2 internal tide signal at each grid point is determined by plane wave analysis using SSH measurements in one fitting window. Plane wave analysis assumes horizontal simple plane waves in 160-km windows or larger, which may be problematic in a complex wave field. Alternatively, Dushaw (2015) maps internal tides in 10° × 10° windows, but the amplitude and phase in each window are spatially variable, because multiple waves of different wavenumbers around the theoretical value are determined. Zaron (2019a) maps M_2 internal tides using 500-km windows, where the polynomial fit is used to allow spatially variable amplitude and phase in one given window.

The present paper explores the feasibility of mapping internal tides using nonrepeat altimetry missions. It reveals that M_2 internal tides can be estimated using 8 years of SSH measurements made mainly by nonrepeat altimetry missions (section 2). There are seven altimetry missions (phases) from 2011 to 2018 and most of them are along drifting long-repeat or geodetic tracks. For example, *CryoSat-2* has 10 668 ground tracks and the *Haiyang-2A* geodetic phase has 4630 ground tracks. The new dataset samples the global internal tide field with different spatial and temporal sampling patterns. The new dataset has advantages in observing the internal tide field, because of its shorter time coverage and denser ground tracks. Thus, the new dataset can be used to examine the impact of the two factors in mapping internal tides. First, its dense ground tracks make it possible to map mode-1 M_2 internal tides using windows as small as 40 km (section 3). Internal tides are thus mapped using different fitting windows, and the results are used to examine the impact of window size. Second, the new dataset is 8 years long from 2011 to 2018, compared to the previous dataset of 25 years long from 1993 to 2017. Results from the two datasets are used to examine the impact of time coverage.

This work is made possible by a recently developed mapping technique (Zhao 2019, 2020, 2021). It consists of two rounds of plane wave analysis with a spatial bandpass filter in between. Plane wave analysis determines internal tidal waves using all SSH measurements in one given window, utilizing the known frequency and wavenumber of the target internal tide. It does not require the SSH measurements to lie along exact-repeat tracks. The spatial two-dimensional (2D) bandpass filter in the second step is indispensable in cleaning the internal tide field. As a result, mode-1 M_2 internal tides are observed from nonrepeat altimetry missions. In contrast, point-wise harmonic analysis cannot extract internal tides from nonrepeat altimetry missions, because the SSH time series at any given point is too short to extract tidal harmonics.

The rest of this paper is arranged as follows. Section 2 describes the two satellite altimetry datasets used in this paper. Section 3 presents the mapping technique. Section 4 presents and compares the resultant internal tide models. It also examines the impact of window size and time coverage on mapping internal tides. Section 5 is a summary.

2. Data

The satellite altimetry data used in this paper are shown in Fig. 1. The two datasets are indicated using two black boxes.

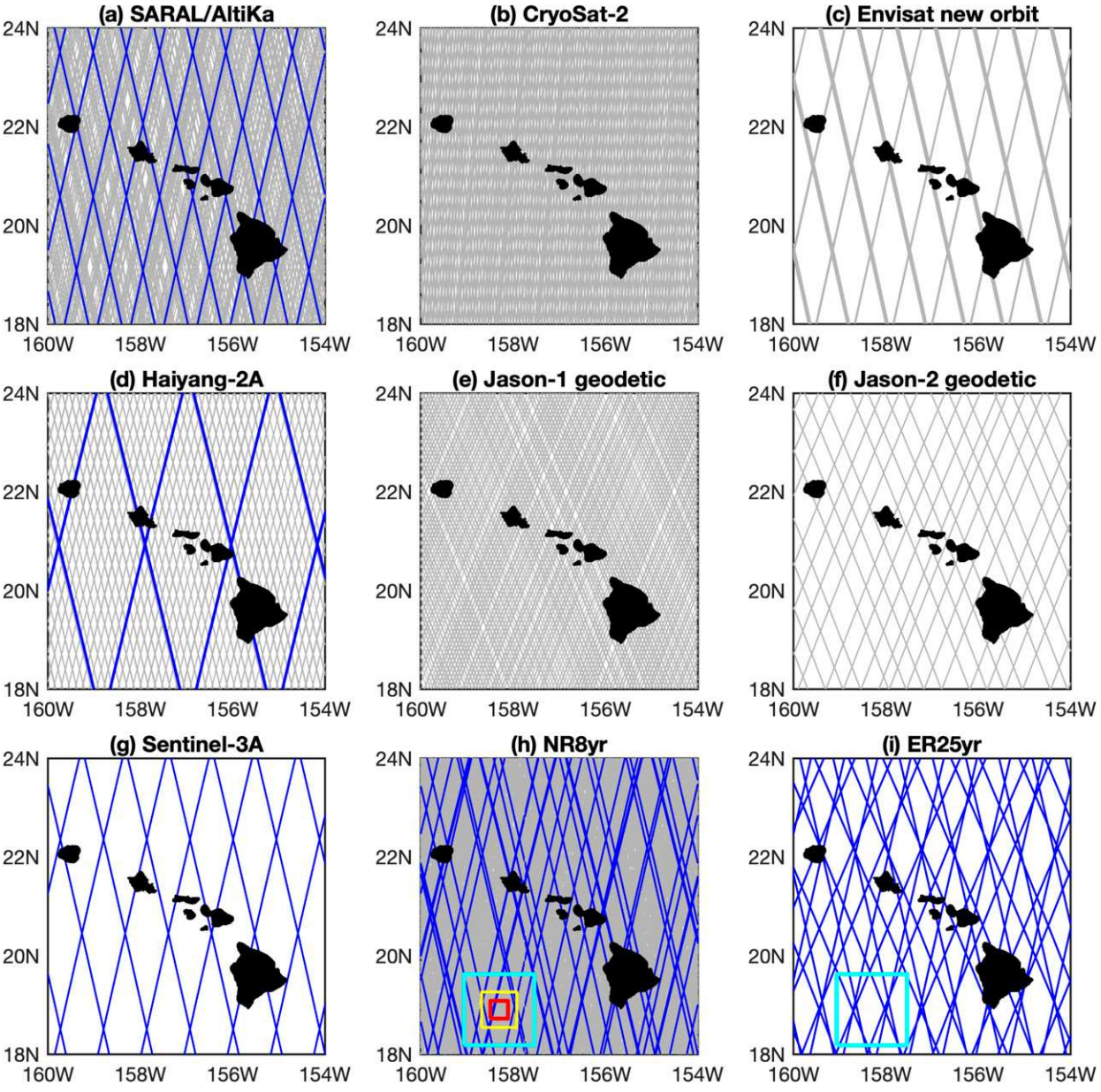

FIG. 2. Ground tracks of the satellite altimetry missions around Hawaii: (a) *SARAL*/AltiKa, (b) *CryoSat-2*, (c) *Envisat* new orbit, (d) *Haiyang-2A*, (e) *Jason-1* geodetic phase, (f) *Jason-2* geodetic phase, (g) *Sentinel-3A*, (h) NR8yr, and (i) ER25yr. Exact-repeat and nonrepeat missions (phases) are in blue and gray, respectively. The cyan, yellow, and red boxes indicate 160-, 80-, and 40-km fitting windows, respectively.

The first dataset is labeled ER25yr, meaning that it is from exact-repeat (ER) missions (phases) with a 25-yr-long time coverage from 1993 to 2017. The missions include TOPEX/Poseidon, *Jason-1*, *Jason-2*, *Jason-3*, *ERS-2*, *Envisat*, and *Geosat Follow-On*. The second dataset is labeled NR8yr, meaning that it is mainly from nonrepeat missions (phases) with an 8-yr-long time coverage from 2011 to 2018. This dataset is from seven missions (phases): *SARAL*/AltiKa, *CryoSat-2*, *Envisat* new orbit, *Haiyang-2A*, *Jason-1* geodetic phase, *Jason-2* geodetic phase, and *Sentinel-3A*. These two datasets have different time coverages and different track patterns. They are totally independent of each other, and the resultant models will be compared in this paper.

The ground tracks of these missions (phases) are shown in Fig. 2. *SARAL*/AltiKa has two phases (Fig. 2a). It runs first along 1002 exact-repeat tracks and then along nonrepeat drifting tracks. *CryoSat-2* has a long repeat period of 369 days and samples the ocean along 10 668 ground tracks (Fig. 2b). *Envisat* new orbit has 1002 ground tracks per cycle, the same as in its normal phase, but the new orbit is loosely controlled

TABLE 1. The mapping procedure. Mode-1 M_2 internal tides are mapped from NR8yr and ER25yr following the same procedure and using the same parameters, except for different windows in the first step. Six different windows are used for NR8yr and only the 160-km window is used for ER25yr. The wavenumber of mode-1 M_2 internal tides K(lon, lat) is calculated using the hydrographic climatology in the *WOA13*.

Procedure	Operation	Key parameters
Step 1	Plane wave analysis	0.2° × 0.2° spatial grid; 40-, 60-, 80-,100-, 120- and 160-km window; 5 waves
Step 2	Spatial bandpass filter	850-km window; bandpass cutoff wavenumbers are [0.75 1.50] × K(lon, lat)
Step 3	Plane wave analysis	0.2° × 0.2° spatial grid; 100-km window; 5 waves

and drifting (Fig. 1c). *Haiyang-2A* has two phases (Fig. 2d). It has 386 ground tracks in the exact-repeat phase and 4630 ground tracks in the geodetic phase. The *Jason-1* geodetic phase lasts for about one year (Fig. 2e). The *Jason-2* geodetic phase lasts for about two months (Fig. 2f). During this period, *Sentinel-3A* is in the exact-repeat phase and along 770 ground tracks (Fig. 2g). The merged dataset NR8yr has much denser ground tracks (Fig. 2h). The dataset ER25yr has 1998 ground tracks (Fig. 2i). In mapping internal tides from discrete ground tracks by plane wave analysis, ER25yr requires 160-km fitting windows. Fortunately, NR8yr can map internal tides in fitting windows from 40 to 160 km.

All SSH measurements have been processed by applying standard corrections for atmospheric effects, surface wave bias, and geophysical effects (Pujol et al. 2016; Taburet et al. 2019). In particular, the barotropic ocean tide, polar tide, solid Earth tide, and loading tide are corrected using theoretical or empirical models. After these corrections, the internal tide variance accounts for about 1% of the total variance of satellite altimetry data (Fig. S1 in the online supplemental material). Measurement errors of these altimetry missions range from 2 to 3 cm (refer to Table 2 in EU Copernicus Marine Service Information 2022). However, the random measurement errors do not affect much the estimates of spatiotemporally coherent internal tides. In fact, the errors in estimating internal tides are mainly from leaked large-scale and mesoscale oceanic signals due to frequency aliasing. Prior mesoscale correction is made on the altimetry data using AVISO mesoscale fields (Ray and Byrne 2010; Ray and Zaron 2016; Zaron 2019a). The fields are gridded daily in time and 0.25° longitude × 0.25° latitude in the horizontal (Pujol et al. 2016). The AVISO mesoscale fields are low-pass filtered with a cutoff wavelength of 200 km following Zaron and Ray (2018). This measure is to remove leaked internal tide signals in the AVISO mesoscale fields.

3. Methods

In this study, mode-1 M_2 internal tides are mapped from the two SSH datasets following a three-step procedure, which consists of two rounds of plane wave analysis with a spatial bandpass filter in between. This mapping technique has been employed and described in previous studies (Zhao 2019, 2020, 2021). Table 1 lists the three steps and some key parameters. The wavenumber of mode-1 M_2 internal tides is one prerequisite parameter. It is obtained by solving the Sturm–Liouville orthogonal equation assuming a rigid-lid surface condition, using ocean stratification climatology in the *World Ocean Atlas 2013* (*WOA13*; Locarnini et al. 2013; Zweng et al. 2013) and ocean depth (Smith and Sandwell 1997). The wavenumber of mode-1 M_2 internal tides is a function of longitude and latitude (Ray and Zaron 2016; Zhao et al. 2016). The local wavenumber is used in each fitting window.

In the first step, mode-1 M_2 internal tides are mapped onto the regular spatial grid from discrete ground tracks by plane wave analysis. An iterative algorithm has been developed to extract five largest internal waves (refer to Fig. 2 in Zhao et al. 2016). Using all measurements in one given fitting window, amplitudes, phases, and propagation directions of target internal tidal waves are determined by the least squares fit in each fitting window. Their sum gives the internal tide solution. In the second step, a spatial bandpass filter is used to clean the internal tide field, taking advantage of the spatially regular internal tide field obtained in the first step. The filter is applied to overlapping 850 km × 850 km windows. The internal tide field is first converted to the 2D wavenumber spectrum by Fourier transform. The spectrum is truncated to [0.75 1.50] times the local wavenumber. The truncated spectrum is converted back to the internal tide field by inverse Fourier transform. One example of the spatial 2D bandpass filter is given in Fig. S2. In the third step, plane wave analysis is employed to decompose the total internal tide field into five internal waves of different propagation directions. The decomposition is conducted in overlapping 100 km × 100 km windows, which is empirically chosen after testing several different windows. After the decomposition, there are five internal waves at each grid point. The five waves are saved separately with their amplitudes, phases, and propagation directions. The multiwave decomposition resolves the complex interference field caused by waves of different propagation direction.

The dataset NR8yr has denser ground tracks, so that mode-1 M_2 internal tides can be mapped using small windows (Fig. 2h). Six different windows are used in the first-round plane wave analysis. They are 40, 60, 80, 100, 120, and 160 km, respectively (Table 1). The 10- and 20-km fitting windows are also tested, but the resultant internal tide models have larger errors (not discussed). For all models, the same windows in step 2 (850 km) and step 3 (100 km) are employed. In the end, six internal tide models are constructed from NR8yr, and labeled NR8yr40km, NR8yr60km, NR8yr80km, NR8yr100km, NR8yr120km, and NR8yr160km, respectively. The dataset ER25yr has sparse ground tracks, so that mode-1 M_2 internal tides are mapped from ER25yr using 160-km windows only (Fig. 2h). The resultant model is labeled ER25yr160km, meaning that it is from dataset ER25yr and mapped in 160-km windows. In

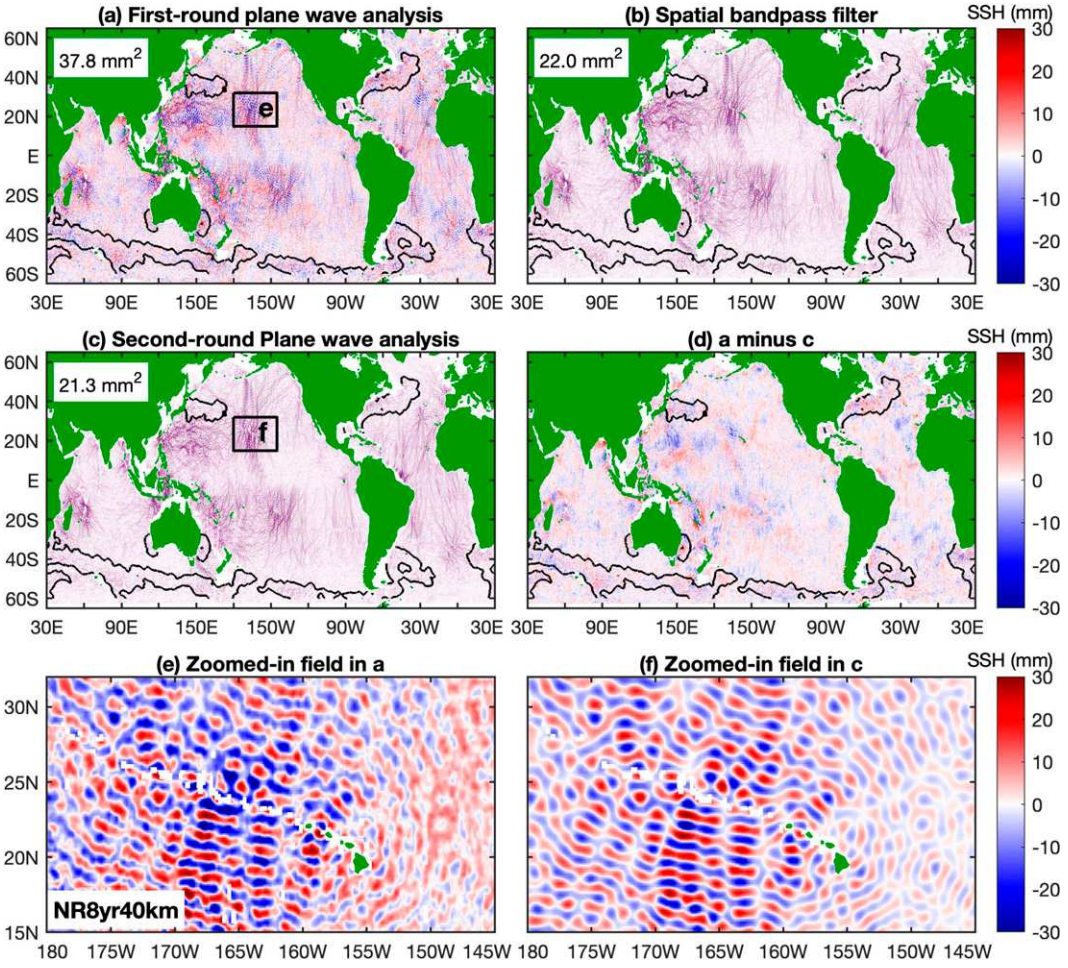

FIG. 3. The mapping procedure. NR8yr40km is shown as an example. (a) The internal tide field obtained by the first-round plane wave analysis. (b) The internal tide field cleaned by spatial 2D bandpass filtering. (c) The internal tide field obtained by the second-round plane wave analysis. (d) The difference between the first- and second-round plane wave analysis. (e),(f) Zoomed-in internal tide field around Hawaii. Internal tides in shallow ocean (<1000 m) are discarded. The black contours indicate regions of strong currents, where internal tides are overwhelmed by leaked large-scale and mesoscale motions. The numbers in (a)–(c) are the global mean model variances (excluding regions of strong currents).

other words, ER25yr160km and NR8yr160km are mapped using same parameters in the three steps, but from ER25yr and NR8yr, respectively. These models will be compared and evaluated using independent satellite altimetry data (section 4). In this study, M_2 internal tides are mapped onto a regular spatial grid of 0.2° longitude × 0.2° latitude. It has been tested that using a higher resolution of 0.1° longitude × 0.1° latitude does not affect these models or conclusions drawn in this paper.

Figure 3 gives one example showing intermediate internal tide fields in this procedure. Internal tide model NR8yr40km is shown here, because it uses the smallest fitting window employed in this paper. Figure 3a shows the mode-1 M_2 internal tide field obtained in the first-round plane wave analysis. Obviously it is overwhelmed by noise in some regions. Figure 3b shows the spatial bandpass filtered internal tide field. It becomes much cleaner. Figure 3c shows the internal tide field obtained by the second-round plane wave analysis. Their global mean variances are 37.8, 22.0, and 21.3 mm^2, respectively. In the second-round plane wave analysis, the variance difference is only 0.7 mm^2 (≈3%). It does not reduce noise much but decomposes the field into five waves at each grid point. Figure 3d shows the difference between Figs. 3a and 3c. Figures 3e and 3f show the zoomed-in internal tide field around Hawaii in the first- and second-round plane wave analysis. It highlights that the mode-1 M_2 internal tide field after the second-round plane wave analysis is much cleaner. The nontidal noise is mainly removed by the spatial bandpass filter in the second step. This feature shows that the spatial bandpass filter is an indispensable step in this procedure. In regions of strong currents (e.g., western boundary currents), satellite altimetric internal tides mapped by this technique are noisy, because of leaked

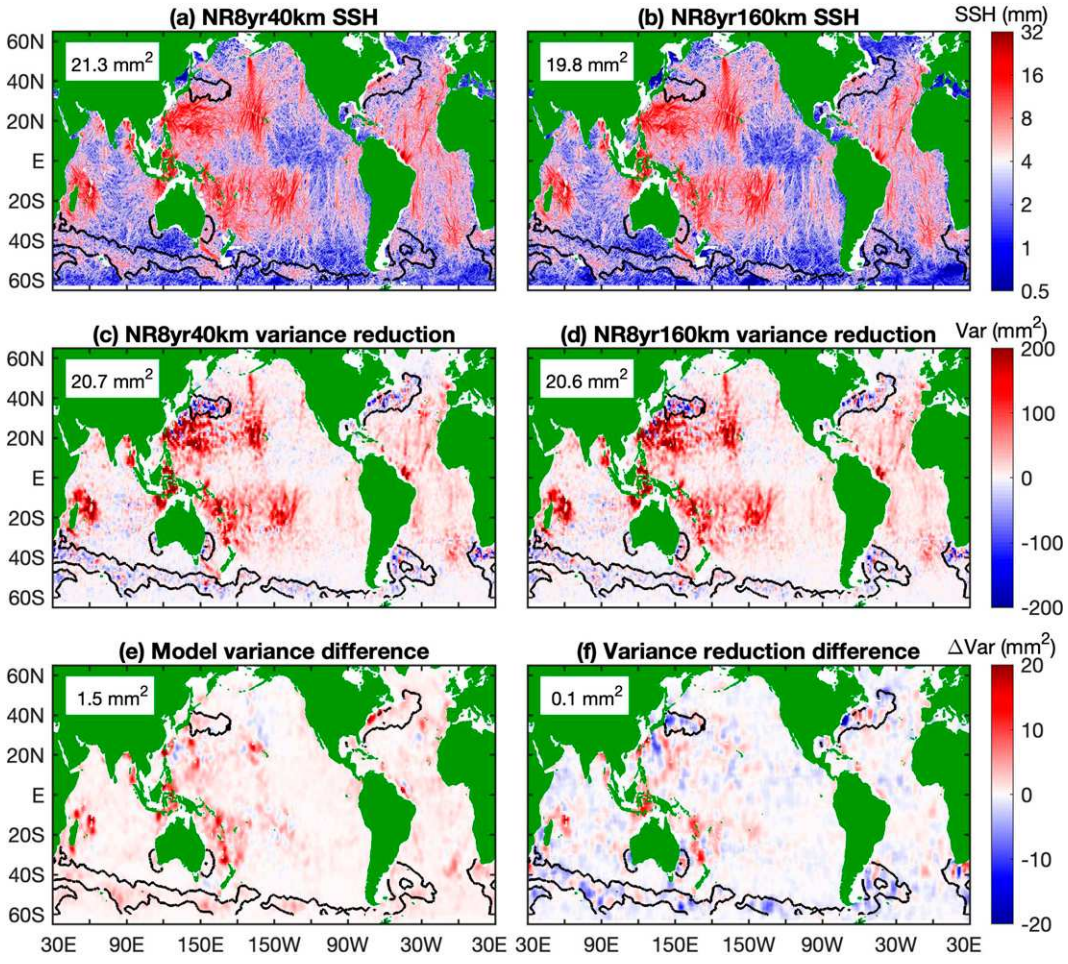

FIG. 4. Mode-1 M_2 internal tide models NR8yr40km and NR8yr160km. (a),(b) SSH amplitudes shown in logarithmic scale. Internal tides in shallow ocean (<1000 m) are discarded (blank). The black contours indicate regions of strong currents, where the satellite altimetric internal tides are noisy. Their global mean variances are calculated and given (excluding regions of strong currents). (c),(d) Model evaluation using the satellite altimetry data in 2020. Shown are variance reduction obtained by making internal tide correction. Their global mean variance reductions are calculated and given (excluding regions of strong currents). (e) Model variance difference of NR8yr40km minus NR8yr160km. (f) Variance reduction difference of NR8yr40km minus NR8yr160km.

large-scale and mesoscale motions (Fig. S1). Internal tides in shallow ocean (<1000 m) are discarded.

4. Results

a. *Internal tide models*

All six mode-1 M_2 internal tide models are shown in Fig. S3. For clarity, Fig. 4 shows only two models, NR8yr40km and NR8yr160km. These two models are chosen because they are mapped using the smallest and largest fitting windows, respectively. The six models have similar spatial patterns. They all demonstrate the basic features of the global mode-1 M_2 internal tide field. There are energetic M_2 internal tides around the Hawaiian Ridge, around the French Polynesian Ridge, in the western Pacific Ocean, in the Madagascar–Mascarene region, and in the Indonesian Seas. These models are consistent with previous observations by satellite altimetry (Ray and Zaron 2016; Zhao et al. 2016; Zaron 2019a; Ubelmann et al. 2022) and numerical simulations (Arbic et al. 2018; Buijsman et al. 2017, 2020; Li and von Storch 2020).

The strength of internal tides is measured in terms of model variance. The global mean model variances of the six models are 21.3, 21.5, 21.6, 21.5, 21.1, and 19.8 mm^2, respectively (Fig. 5). The first five models (excluding NR8yr160km) have very close model variances 21.4 ± 0.3 mm^2, or ±1.5%, while NR8yr160km (19.8 mm^2) has notable lower model variance than NR8yr40km (21.3 mm^2) by 1.5 mm^2 or 7.5%. The large difference between NR8yr40km and NR8yr160km will be studied below. In addition, the SSH amplitudes of the six models are compared with one another. The two-dimensional histograms for all model pairs are shown in Fig. S4. Their root-mean-square (RMS) differences are very small, ranging from 0.5 to 1.1 mm. In summary, the six

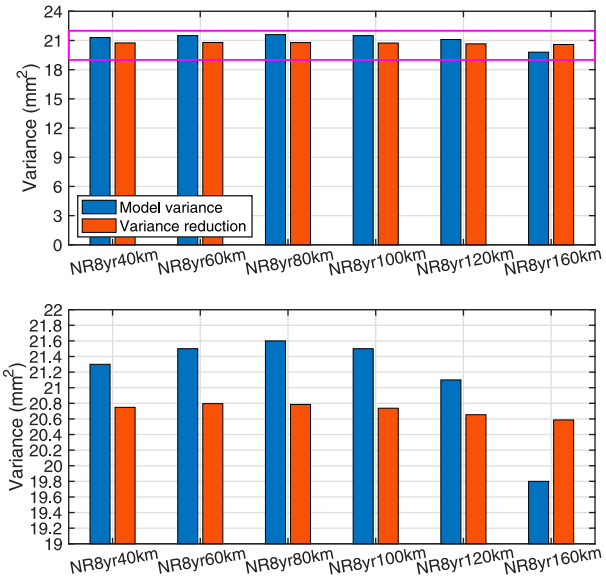

FIG. 5. Global mean model variances and variance reductions. The variance reductions are obtained by making internal tide correction to the satellite altimetry data in 2020. The bottom panel is a zoomed-in view of the top panel. The six NR8yr models mapped with different windows have similar performances on global average.

NR8yr models agree very well in terms of spatial pattern and model variance.

b. *Model evaluation*

The six models are evaluated using the satellite altimetry data in 2020. The 2020 data are merged from six missions: *Sentinel-3A*, *Sentinel-3B*, *Jason-3*, *Haiyang-2B*, *CryoSat-2*, and *SARAL*/AltiKa. The evaluation method has been used in previous studies (Ray and Zaron 2016; Zaron 2019a; Zhao 2021; Carrere et al. 2021). For each SSH measurement of known time and location, the internal tide signal is predicted using the model under evaluation, and subtracted from the raw satellite data. The variance reduction is the difference before and after the internal tide correction. In the end, the variance reductions for all SSH measurements are binned into half-overlapping $2° \times 2°$ windows on a regular grid of $1°$ longitude $\times$ $1°$ latitude.

The global variance reduction maps of the six models are shown in Fig. S5. For clarity, Fig. 4 shows only the variance reductions of NR8yr40km and NR8yr160km. It shows that large variance reductions are usually in regions of strong internal tides such as around the Hawaiian Ridge, the Polynesian Ridge, and in the western Pacific Ocean. These results are consistent with previous studies (Ray and Zaron 2016; Zaron 2019a; Zhao 2021; Carrere et al. 2021). All models cause positive variance reductions in the global ocean, indicating that they are overall good internal tide models. The global mean variance reductions of the six models are 20.7, 20.8, 20.8, 20.7, 20.7, and 20.6 mm^2, respectively. Figure 5 shows a histogram of variance reductions for direct comparison. It reveals that the six models have very close variance reductions (20.7 $\pm$ 0.1 mm^2, or $\pm$0.5%), suggesting that the six models have similar performances in making internal tide correction. Thus, one can conclude that mode-1 M_2 internal tides can be extracted from 8 years of altimetry data made by nonrepeat missions.

c. *Impact of window size*

The impact of window size on mapping internal tides from satellite altimetry is studied by comparing NR8yr40km and NR8yr160km. For this goal, their difference maps of model variance and variance reduction are shown in Figs. 4e and 4f, respectively. Figure 4e shows that NR8yr40km has larger model variance than NR8yr160km throughout the global ocean. In particular, NR8yr40km has larger model variance in strong source regions such as the Hawaiian Ridge, the Madagascar–Mascarene region, the Andaman Sea, the Indonesian Seas, the Izu–Bonin–Mariana arc system, and Meteor Rise in the South Atlantic Ocean. This is reasonable, because NR8yr40km is constructed by fitting plane waves in 40-km small windows, which better resolves those isolated generation sites and leads to larger SSH amplitudes. In contrast, for open-ocean internal tides away from their generation sources, the 40- and 160-km windows do not make much difference.

Figure 4f shows the variance reduction difference between NR8yr40km and NR8yr160km. It shows that NR8yr40km reduces more variance in regions of strong sources listed above (red patches), while NR8yr160km reduces more variance in the open ocean (blue patches). This feature can be explained as follows. Plane wave analysis extracts internal tides using all SSH measurements in one fitting window. A larger fitting window includes more independent SSH measurements (Fig. 2h) and better reduces background nontidal noise. Note that mode-1 M_2 internal tides account for about 1% of SSH variance in the satellite altimetry data (Fig. S1). In regions of strong sources, the 40-km window leads to larger internal tides (than nontidal noise), so that NR8yr40km reduces more variance. In the open ocean with weak internal tides, the 40-km window leads to larger nontidal noise (than internal tides), so that NR8yr40km reduces less variance. In summary, the impact of window size is a function of location. It is a trade-off of competing internal tides and background noise (Fig. S1). For the 8 years of nonrepeat altimetry data, the small 40-km window slightly improves the internal tide model in strong source regions, but slightly worsens the internal tide model in regions of weak internal tides.

d. *Impact of time coverage*

The impact of time coverage is studied by comparing NR8yr160km and ER25yr160km (Fig. 6). These two models are developed from the 8-yr-long (2011–18) and 25-yr-long (1993–2017) datasets following the same procedure and using the same parameters (section 3). The SSH amplitudes of NR8yr160km and ER25yr160km have a considerable RMS difference of 3.1 mm (Fig. S6). Their global mean model variances are 19.8 and 16.5 mm^2 (Figs. 6a,b), respectively, with a difference of 3.3 mm^2 ($\approx$18%). In making internal tide correction to the satellite altimetry data in 2020, their global mean variance reductions are 20.6 and 18.7 mm^2 (Figs. 6c,d),

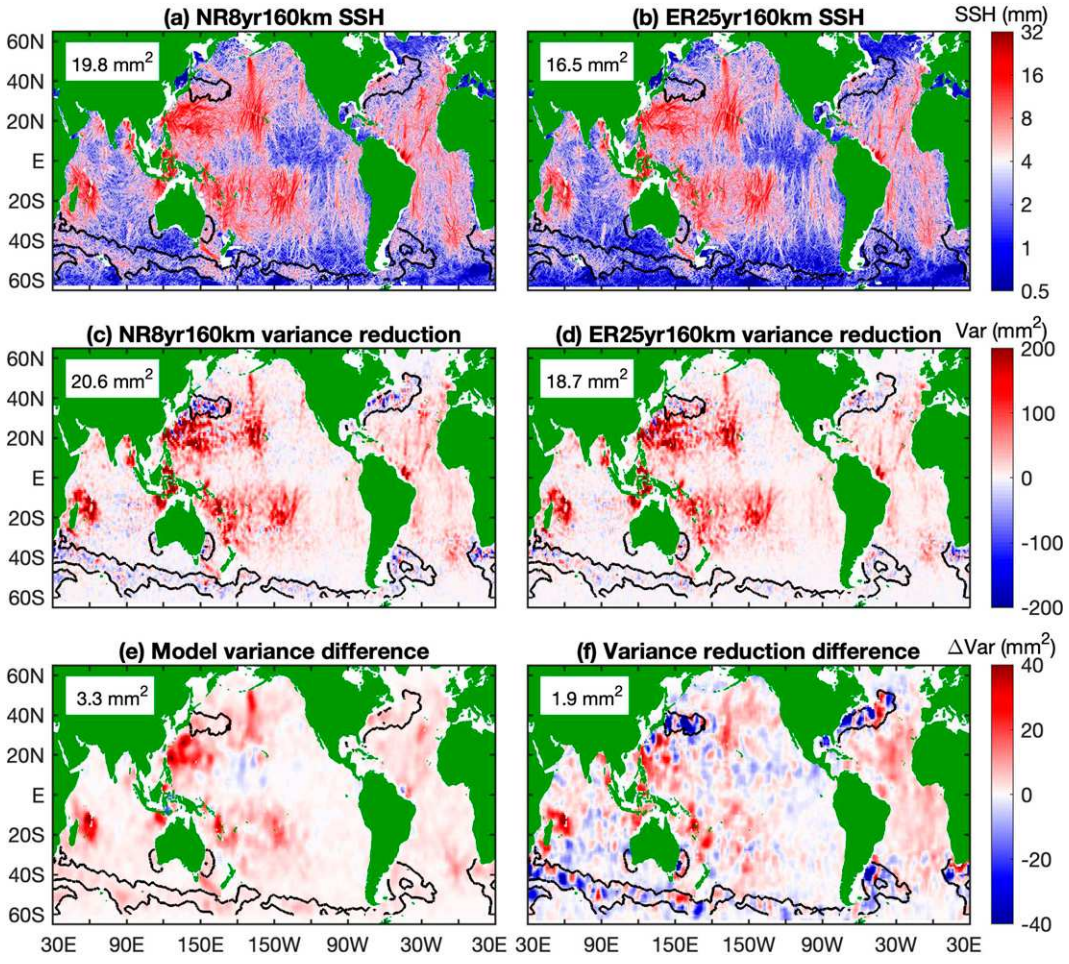

FIG. 6. Mode-1 M_2 internal tide models NR8yr160km and ER25yr160km. (a),(b) SSH amplitudes shown in logarithmic scale. Internal tides in shallow ocean (<1000 m) are discarded (blank). The black contours indicate regions of strong currents, where the satellite altimetric internal tides are noisy. Their global mean variances are calculated and given (excluding regions of strong currents). (c),(d) Model evaluation using the satellite altimetry data in 2020. Shown are variance reduction obtained by making internal tide correction. Their global mean variance reductions are calculated and given (excluding regions of strong currents). (e) Model variance difference of NR8yr160km minus ER25yr160km. (f) Variance reduction difference of NR8yr160km minus ER25yr160km.

respectively, with a difference of 1.9 mm^2 (≈10%). Figure 6e gives their difference map of model variance. It shows that NR8yr160km has larger model variance than ER25yr160km throughout the global ocean, particularly in regions of strong internal tides. Figure 6f gives their difference map of variance reduction. It shows that NR8yr160km has larger variance reduction than ER25yr160km in regions of strong internal tides. In summary, NR8yr160km has significantly larger model variance and larger variance reduction than ER25yr160km. However, prior to drawing the conclusion that NR8yr160km is a better internal tide model, two possibilities must be ruled out.

First, one might think that NR8yr160km contains S_2 internal tides, which may lead to larger model variance and larger variance reduction. Two pieces of analyses are conducted to rule out this possibility. 1) S_2 internal tides are specifically extracted from the M_2 internal tide model NR8yr160km following the same procedure in this paper (section 3). The S_2 internal tide model (NR8yr160km-S_2) and M_2 internal tide model (NR8yr160km) are shown in Fig. S7. It shows that their model variances are 0.028 and 19.8 mm^2, respectively, with a ratio of ≈1/700, suggesting that NR8yr160km contains negligible S_2 internal tides. 2) The satellite altimetry data in 2020 are preprocessed by subtracting S_2 internal tides using one existing S_2 internal tide model (Zhao 2017). Then, NR8yr160km is evaluated using the raw and corrected 2020 data. The resultant variance reductions are shown in Fig. S8. The results shows that the raw and corrected data yield close variance reductions (20.6 vs 20.7 mm^2), confirming that NR8yr160km contains negligible S_2 internal tides.

Second, one might wonder whether NR8yr160km performs better than ER25yr160km for other satellite altimetry data or not. To address this concern, NR8yr160km and ER25yr160km are compared using four sets of satellite altimetry data. The 2020 data are from six altimetry missions as described in

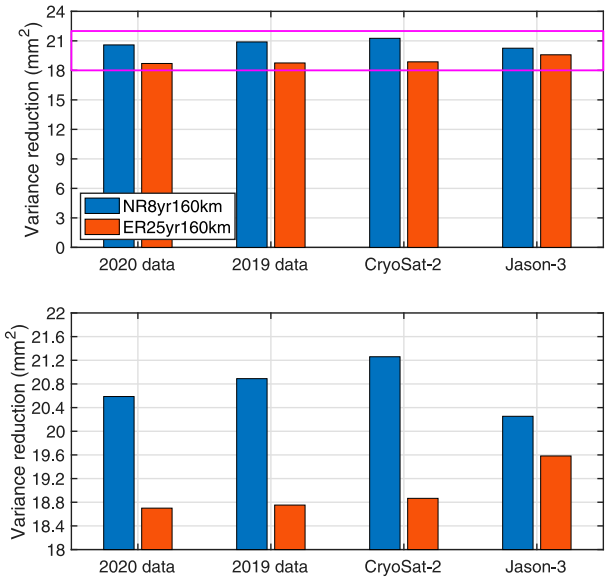

FIG. 7. Variance reductions of NR8yr160km and ER25yr160km in making internal tide correction to four sets of satellite altimetry data. The bottom panel is a zoomed-in view of the top panel. The 2019 data are from six altimetry missions in 2019. The 2020 data are from six altimetry missions in 2020. The *CryoSat-2* data are from 2019 and 2020. The *Jason-3* data are from 2019 and 2020. NR8yr160km performs better than ER25yr160km for all four datasets.

section 4b. The 2019 data are from six altimetry missions: *Sentinel-3A*, *Sentinel-3B*, *Jason-3*, *Haiyang-2A*, *CryoSat-2*, and *SARAL*/AltiKa. The *CryoSat-2* data are from 2019 and 2020. The *Jason-3* data are from 2019 and 2020. The same procedure as described in section 4b are used to evaluate the two models. The resultant variance reduction maps are shown in Figs. S9 and S10. Figure 7 gives a summary of their global mean variance reductions. The results show that NR8yr160km performs better than ER25yr160km for all four datasets, though by different degrees (Fig. S11). Note that the 25 years of TOPEX/Poseidon and *Jason-1*/*-2*/*-3* data (1993–2017) have been used in constructing ER25yr160km. The *Jason-3* data from 2019 and 2020 used in the evaluation are sampled along the same ground tracks; therefore, the Jason-3 data are not completely independent, but favor ER25yr160km. Thus, NR8yr160km performs better than ER25yr160km by a low degree (0.7 mm^2 or 3%). On the contrary, the *CryoSat-2* data favor NR8yr160km, because the 8 years of *CryoSat-2* data (2011–18) have been used in constructing NR8yr160km. Thus, NR8yr160km performs better by a high degree (2.4 mm^2 or 12%). For comparison, NR8yr160km performs better than ER25yr160km for the 2019 and 2020 data by 2.1 mm^2 (11%) and 1.9 mm^2 (10%), respectively (Fig. 7). The results confirm that NR8yr160km performs better than ER25yr160km for all satellite altimetry data, even for the *Jason-3* data that favor ER25yr160km.

This analysis proves the following statements: NR8yr160km contains negligible S_2 internal tides, NR8yr160km has larger model variance than ER25yr160km, and NR8yr160km performs better than ER25yr160km in making internal tide correction. In conclusion, NR8yr160km is a better internal tide model than ER25yr160km on global average. It is because this model is constructed using 8 years of data made by nonrepeat altimetry missions, in contrast to 25 years of data made by exact-repeat altimetry missions.

e. *Internal tide energy*

The depth-integrated internal tide energy E is calculated from the SSH amplitude η following $E = (1/2)E_n\eta^2$, where E_n is a transfer function from η to E. Here, E_n is a function of tidal frequency, latitude, mode number, ocean stratification, and ocean depth (Zhao et al. 2016). The E_n for mode-1 M_2 internal tides has been computed and shown in Fig. A2 in Zhao et al. (2016). There are five internal tidal waves at each grid point. The energies of the five waves are separately calculated, and their sum gives the total internal tide energy at this grid point. Furthermore, the globally integrated area-weighted internal tide energy is calculated following Zhao et al. (2016). In the calculation, the decrease in the spheric area with increasing latitude is taken into account. The global energy maps of the six NR8yr internal tide models are shown in Fig. S12. They have similar spatial patterns, consistent with their similar patterns in amplitude (Fig. 4). Figure 8 shows that the global energy maps of NR8yr160km and ER25yr160km. Large energies are usually associated with strong generation sites, consistent with previous studies (Zhao et al. 2016; Zaron et al. 2022). Long-range internal tides can be seen in both maps. It is hard to see their difference (in logarithmic scale) by visual examination of the two maps. The difference map of NR8yr160km and ER25yr160km is shown in Fig. 8c.

The global energies of NR8yr160km and ER25yr160km are 43.6 and 33.6 PJ, respectively, with a different of 10 PJ. NR8yr160km has higher energy than ER25yr160km, mainly because the former represents an 8-yr-coherent field while the latter a 25-yr-coherent field. Figure 8 shows some noteworthy features. The energy difference between NR8yr160km and ER25yr160km is a function of location. The difference is generally small in the equatorial zone, because the internal tides themselves are weak in the equatorial zone. The energy difference at high latitudes is noisy, because the transfer function E_n increases sharply with internal tides getting close to turning latitudes 75.3°S/N. The integrated energy from 52°S to 52°N (excluding higher latitudes) is 7.8 PJ, compared to 10 PJ globally. There are two large differences in regions including the internal tides from Amukta Pass, Alaska, and the Macquarie Ridge (Fig. 8, blue boxes). This feature suggests that the internal tides in these regions are subject to strong interannual variability. There is one anomalous feature: NR8yr160km has slightly lower energy than ER25yr160km to the south of Hawaii, likely also due to interannual variability (Zhao 2022). A study of their different features is interesting, but beyond the scope of this paper.

5. Summary

Satellite altimetry offers a unique technique for observing internal tides on a global scale. However, previous satellite

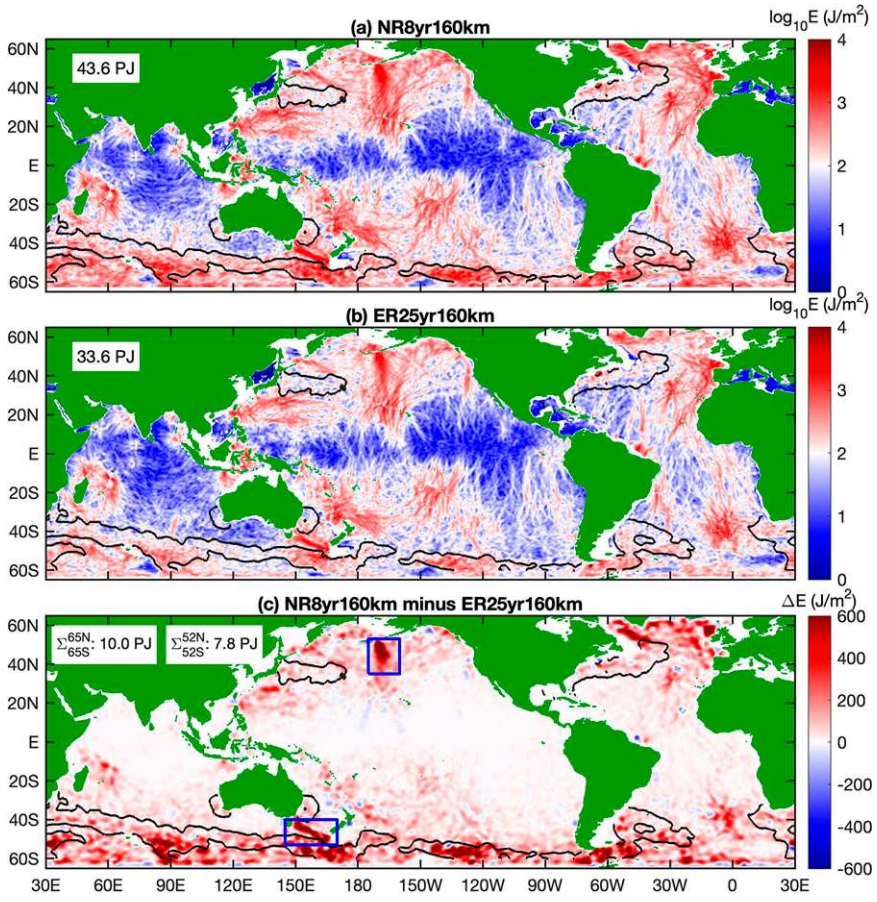

FIG. 8. Depth-integrated internal tide energy. (a) NR8yr160km, (b) ER25yr160km, and (c) NR8yr160km minus ER25yr160km. The black contours indicate regions of strong currents, where the satellite altimetric internal tides are noisy. Their globally integrated energies (or differences) are calculated and given (excluding regions of strong currents).

observations of internal tides are mainly based on about 25 years of SSH measurements (1993–2017) made by exact-repeat altimetry missions (phases). These missions have sparse ground tracks. As a result, large fitting windows are needed in mapping internal tides. In this study, mode-1 M_2 internal tides have been estimated using 8 years of SSH measurements (2011–18) made mainly by nonrepeat altimetry missions (phases). The two datasets are labeled ER25yr and NR8yr, respectively. NR8yr has advantages over ER25yr in mapping internal tides, because NR8yr has dense ground tracks and short time coverage.

This work has been made possible by a new mapping technique (Zhao 2019, 2020, 2021). The new technique consists of two rounds of plane wave analysis with a spatial bandpass filter in between. Plane wave analysis determines internal tidal waves using all SSH measurements in one given window, utilizing known frequency and wavenumber. It does not require the SSH measurements to lie along exact-repeat tracks. In contrast, point-wise harmonic analysis cannot extract internal tides from nonrepeat missions, because the SSH time series at any given point is too short to determine robust harmonic constants.

Taking advantage of the denser ground tracks of NR8yr, M_2 internal tides are mapped using six different fitting windows. They are 40-, 60-, 80-, 100-, 120-, and 160-km windows, respectively. The resultant six internal tide models agree with one another very well in terms of spatial pattern and model variance. Evaluation using the independent altimetry data in 2020 shows that they have similar performances in reducing variance. On global average, the size of fitting window does not make much difference. However, small fitting windows can better resolve internal tides in isolated strong source regions. The results show that M_2 internal tides can be mapped using the 8-yr-long SSH measurements made by nonrepeat altimetry missions.

The impact of time coverage is studied by comparing internal tide models NR8yr160km and ER25yr160km, which are mapped from datasets NR8yr and ER25yr using same mapping parameters. NR8yr160km proves to be a better internal tide model, because 1) it has larger model variance and 2) it reduces more variance in making internal tide correction to four sets of satellite altimetry data. NR8yr160km represents an 8-yr coherent field, while ER25yr160km is a 25-yr coherent

field. Their global energies are 43.6 and 33.6 PJ, respectively, indicating that ER25yr160km underestimates M_2 internal tides by about 10 PJ. A comparison of the two internal tide models sheds light on the spatiotemporal variation of internal tides on a global scale.

Acknowledgments. This work was supported by the National Aeronautics and Space Administration (NASA) via Projects NNX17AH57G and 80NSSC18K0771, and the National Science Foundation (NSF) via Projects OCE1947592 and OCE2149028.

Data availability statement. The satellite altimetry along-track data were downloaded from the Copernicus Marine Service (https://doi.org/10.48670/moi-00146). The satellite altimetry gridded data were also downloaded from the Copernicus Marine Service (https://doi.org/10.48670/moi-00148). The *World Ocean Atlas 2013* is produced and made available by NOAA National Oceanographic Data Center (https://www.nodc.noaa.gov/OC5/woa13/). Internal tide models developed in this paper can be downloaded from https://doi.org/10.6084/m9.figshare.21453588.v1.

REFERENCES

Arbic, B., and Coauthors, 2018: A primer on global internal tide and internal gravity wave continuum modeling in HYCOM and MITgcm. *New Frontiers in Operational Oceanography*, E. Chassignet et al., Eds., GODAE OceanView, 307–392, https://doi.org/10.17125/gov2018.ch13.

Buijsman, M. C., B. K. Arbic, J. G. Richman, J. F. Shriver, A. J. Wallcraft, and L. Zamudio, 2017: Semidiurnal internal tide incoherence in the equatorial Pacific. *J. Geophys. Res. Oceans*, **122**, 5286–5305, https://doi.org/10.1002/2016JC012590.

——, and Coauthors, 2020: On the interplay between horizontal resolution and wave drag and their effect on tidal baroclinic mode waves in realistic global ocean simulations. *Ocean Modell.*, **152**, 101656, https://doi.org/10.1016/j.ocemod.2020.101656.

Cacchione, D. A., L. F. Praston, and A. S. Ogston, 2002: The shaping of continental slopes by internal tides. *Science*, **296**, 724–727, https://doi.org/10.1126/science.1069803.

Carrere, L., and Coauthors, 2021: Accuracy assessment of global internal tide models using satellite altimetry. *Ocean Sci.*, **17**, 147–180, https://doi.org/10.5194/os-17-147-2021.

de Lavergne, C., and Coauthors., 2020: A parameterization of local and remote tidal mixing. *J. Adv. Model. Earth Syst.*, **12**, e2020MS002065, https://doi.org/10.1029/2020MS002065.

Dunphy, M., A. L. Ponte, P. Klein, and S. Le Gentil, 2017: Low-mode internal tide propagation in a turbulent eddy field. *J. Phys. Oceanogr.*, **47**, 649–665, https://doi.org/10.1175/JPO-D-16-0099.1.

Dushaw, B. D., 2015: An empirical model for mode-1 internal tides derived from satellite altimetry: Computing accurate tidal predictions at arbitrary points over the world oceans. Tech. Memo. APL-UW 1-15, Applied Physics Laboratory, University of Washington, 114 pp., https://apl.uw.edu/project/projects/tm_1-15/pdfs/tm_1_15.pdf.

Egbert, G. D., and R. D. Ray, 2000: Significant dissipation of tidal energy in the deep ocean inferred from satellite altimeter data. *Nature*, **405**, 775–778, https://doi.org/10.1038/35015531.

EU Copernicus Marine Service Information, 2022: Quality Information Document (CMEMS-SL-QUID-008-032-068). 72 pp., EU Copernicus Marine Service Information, https://doi.org/10.48670/moi-00146.

Garrett, C., and E. Kunze, 2007: Internal tide generation in the deep ocean. *Annu. Rev. Fluid Mech.*, **39**, 57–87, https://doi.org/10.1146/annurev.fluid.39.050905.110227.

Jayne, S. R., and L. C. St. Laurent, 2001: Parameterizing tidal dissipation over rough topography. *Geophys. Res. Lett.*, **28**, 811–814, https://doi.org/10.1029/2000GL012044.

Kelly, S. M., P. F. J. Lermusiaux, T. F. Duda, and P. J. Haley Jr., 2016: A coupled-mode shallow-water model for tidal analysis: Internal tide reflection and refraction by the Gulf Stream. *J. Phys. Oceanogr.*, **46**, 3661–3679, https://doi.org/10.1175/JPO-D-16-0018.1.

——, A. F. Waterhouse, and A. C. Savage, 2021: Global dynamics of the stationary M_2 mode-1 internal tide. *Geophys. Res. Lett.*, **48**, e2020GL091692, https://doi.org/10.1029/2020GL091692.

Li, Z., and J.-S. von Storch, 2020: M_2 internal-tide generation in STORMTIDE2. *J. Geophys. Res. Oceans*, **125**, e2019JC015453, https://doi.org/10.1029/2019JC015453.

Löb, J., J. Köhler, C. Mertens, M. Walter, Z. Li, J.-S. von Storch, Z. Zhao, and M. Rhein, 2020: Observations of the low-mode internal tide and its interaction with mesoscale flow south of the Azores. *J. Geophys. Res. Oceans*, **125**, e2019JC015879, https://doi.org/10.1029/2019JC015879.

Locarnini, R. A., and Coauthors, 2013: *Temperature*. Vol. 1, *World Ocean Atlas 2013*, NOAA Atlas NESDIS 73, 40 pp., http://data.nodc.noaa.gov/woa/WOA13/DOC/woa13_vol1.pdf.

MacKinnon, J. A., and Coauthors, 2017: Climate process team on internal wave-driven ocean mixing. *Bull. Amer. Meteor. Soc.*, **98**, 2429–2454, https://doi.org/10.1175/BAMS-D-16-0030.1.

Olbers, D., F. Pollmann, and C. Eden, 2020: On PSI interactions in internal gravity wave fields and the decay of baroclinic tides. *J. Phys. Oceanogr.*, **50**, 751–771, https://doi.org/10.1175/JPO-D-19-0224.1.

Pollmann, F., J. Nycander, C. Eden, and D. Olbers, 2019: Resolving the horizontal direction of internal tide generation. *J. Fluid Mech.*, **864**, 381–407, https://doi.org/10.1017/jfm.2019.9.

Ponte, A. L., and P. Klein, 2015: Incoherent signature of internal tides on sea level in idealized numerical simulations. *Geophys. Res. Lett.*, **42**, 1520–1526, https://doi.org/10.1002/2014GL062583.

Pujol, M.-I., Y. Faugère, G. Taburet, S. Dupuy, C. Pelloquin, M. Ablain, and N. Picot, 2016: DUACS DT2014: The new multi-mission altimeter data set reprocessed over 20 years. *Ocean Sci.*, **12**, 1067–1090, https://doi.org/10.5194/os-12-1067-2016.

Ray, R. D., and D. E. Cartwright, 2001: Estimates of internal tide energy fluxes from TOPEX/Poseidon altimetry: Central North Pacific. *Geophys. Res. Lett.*, **28**, 1259–1262, https://doi.org/10.1029/2000GL012447.

——, and D. A. Byrne, 2010: Bottom pressure tides along a line in the southeast Atlantic Ocean and comparisons with satellite altimetry. *Ocean Dyn.*, **60**, 1167–1176, https://doi.org/10.1007/s10236-010-0316-0.

——, and E. D. Zaron, 2011: Non-stationary internal tides observed with satellite altimetry. *Geophys. Res. Lett.*, **38**, L17609, https://doi.org/10.1029/2011GL048617.

——, and ——, 2016: M_2 internal tides and their observed wavenumber spectra from satellite altimetry. *J. Phys. Oceanogr.*, **46**, 3–22, https://doi.org/10.1175/JPO-D-15-0065.1.

Rudnick, D. L., and Coauthors, 2003: From tides to mixing along the Hawaiian Ridge. *Science*, **301**, 355–357, https://doi.org/10.1126/science.1085837.

Sasaki, H., S. Kida, R. Furue, M. Nonaka, and Y. Masumoto, 2018: An increase of the Indonesian throughflow by internal tidal mixing in a high-resolution quasi-global ocean simulation. *Geophys. Res. Lett.*, **45**, 8416–8424, https://doi.org/10.1029/2018GL078040.

Savage, A. C., A. F. Waterhouse, and S. M. Kelly, 2020: Internal tide nonstationarity and wave-mesoscale interactions in the Tasman Sea. *J. Phys. Oceanogr.*, **50**, 2931–2951, https://doi.org/10.1175/JPO-D-19-0283.1.

Shakespeare, C. J., 2020: Interdependence of internal tide and lee wave generation at abyssal hills: Global calculations. *J. Phys. Oceanogr.*, **50**, 655–677, https://doi.org/10.1175/JPO-D-19-0179.1.

Smith, W. H. F., and D. T. Sandwell, 1997: Global sea floor topography from satellite altimetry and ship depth soundings. *Science*, **277**, 1956–1962, https://doi.org/10.1126/science.277.5334.1956.

Taburet, G., A. Sanchez-Roman, M. Ballarotta, M.-I. Pujol, J.-F. Legeais, F. Fournier, Y. Faugere, and G. Dibarboure, 2019: DUACS DT2018: 25 years of reprocessed sea level altimetry products. *Ocean Sci.*, **15**, 1207–1224, https://doi.org/10.5194/os-15-1207-2019.

Ubelmann, C., L. Carrere, C. Durand, G. Dibarboure, Y. Faugère, M. Ballarotta, F. Briol, and F. Lyard, 2022: Simultaneous estimation of ocean mesoscale and coherent internal tide sea surface height signatures from the global altimetry record. *Ocean Sci.*, **18**, 469–481, https://doi.org/10.5194/os-18-469-2022.

Vic, C., and Coauthors, 2019: Deep-ocean mixing driven by small-scale internal tides. *Nat. Commun.*, **10**, 2099, https://doi.org/10.1038/s41467-019-10149-5.

——, B. Ferron, V. Thierry, H. Mercier, and P. Lherminier, 2021: Tidal and near-inertial internal waves over the Reykjanes Ridge. *J. Phys. Oceanogr.*, **51**, 419–437, https://doi.org/10.1175/JPO-D-20-0097.1.

Whalen, C. B., C. de Lavergne, A. C. Naveira Garabato, J. M. Klymak, J. A. MacKinnon, and K. L. Sheen, 2020: Internal wave-driven mixing: Governing processes and consequences for climate. *Nat. Rev. Earth Environ.*, **1**, 606–621, https://doi.org/10.1038/s43017-020-0097-z.

Wunsch, C., 1975: Internal tides in the ocean. *Rev. Geophys. Space Phys.*, **13**, 167–182, https://doi.org/10.1029/RG013i001p00167.

Zaron, E. D., 2019a: Baroclinic tidal sea level from exact-repeating mission altimetry. *J. Phys. Oceanogr.*, **49**, 193–210, https://doi.org/10.1175/JPO-D-18-0127.1.

——, 2019b: Predictability of non-phase-locked baroclinic tides in the Caribbean Sea. *Ocean Sci.*, **15**, 1287–1305, https://doi.org/10.5194/os-15-1287-2019.

——, and G. D. Egbert, 2014: Time-variable refraction of the internal tide at the Hawaiian ridge. *J. Phys. Oceanogr.*, **44**, 538–557, https://doi.org/10.1175/JPO-D-12-0238.1.

——, and R. D. Ray, 2018: Aliased tidal variability in mesoscale sea level anomaly maps. *J. Atmos. Oceanic Technol.*, **35**, 2421–2435, https://doi.org/10.1175/JTECH-D-18-0089.1.

——, R. C. Musgrave, and G. D. Egbert, 2022: Baroclinic tidal energetics inferred from satellite altimetry. *J. Phys. Oceanogr.*, **52**, 1015–1032, https://doi.org/10.1175/JPO-D-21-0096.1.

Zhao, Z., 2016: Internal tide oceanic tomography. *Geophys. Res. Lett.*, **43**, 9157–9164, https://doi.org/10.1002/2016GL070567.

——, 2017: The global mode-1 S_2 internal tide. *J. Geophys. Res. Oceans*, **122**, 8794–8812, https://doi.org/10.1002/2017JC013112.

——, 2019: Mapping internal tides from satellite altimetry without blind directions. *J. Geophys. Res. Oceans*, **124**, 8605–8625, https://doi.org/10.1029/2019JC015507.

——, 2020: Southward internal tides in the northeastern South China Sea. *J. Geophys. Res. Oceans*, **125**, e2020JC01654, https://doi.org/10.1029/2020JC016554.

——, 2021: Seasonal mode-1 M_2 internal tides from satellite altimetry. *J. Phys. Oceanogr.*, **51**, 3015–3035, https://doi.org/10.1175/JPO-D-21-0001.1.

——, 2022: Development of the yearly mode-1 M_2 internal tide model in 2019. *J. Atmos. Oceanic Technol.*, **39**, 463–478, https://doi.org/10.1175/JTECH-D-21-0116.1.

——, and M. H. Alford, 2009: New altimetric estimates of mode-1 M_2 internal tides in the central North Pacific Ocean. *J. Phys. Oceanogr.*, **39**, 1669–1684, https://doi.org/10.1175/2009JPO3922.1.

——, ——, J. B. Girton, L. Rainville, and H. L. Simmons, 2016: Global observations of open-ocean mode-1 M_2 internal tides. *J. Phys. Oceanogr.*, **46**, 1657–1684, https://doi.org/10.1175/JPO-D-15-0105.1.

——, J. Wang, D. Menemenlis, L.-L. Fu, S. Chen, and B. Qiu, 2019: Decomposition of the multimodal multidirectional M_2 internal tide field. *J. Atmos. Oceanic Technol.*, **36**, 1157–1173, https://doi.org/10.1175/JTECH-D-19-0022.1.

Zweng, M., and Coauthors, 2013: *Salinity*. Vol. 2, *World Ocean Atlas 2013*, NOAA Atlas NESDIS 74, 39 pp., http://data.nodc.noaa.gov/woa/WOA13/DOC/woa13_vol2.pdf.